



Protosolar D-to-H Abundance and One Part per Billion PH₃ in the Coldest Brown Dwarf

Melanie J. Rowland¹ , Caroline V. Morley¹ , Brittany E. Miles^{2,22} , Genaro Suarez³ , Jacqueline K. Faherty³ , Andrew J. Skemer⁴ , Samuel A. Beiler⁵ , Michael R. Line⁶ , Gordon L. Bjoraker⁷ , Jonathan J. Fortney⁴ , Johanna M. Vos⁸ , Shereilyn Alejandro Merchan^{3,9} , Mark Marley¹⁰ , Ben Burningham¹¹ , Richard Freedman¹² , Ehsan Gharib-Nezhad^{13,14} , Natasha Batalha¹³ , Roxana Lupu¹⁵ , Channon Visscher^{16,17} , Adam C. Schneider¹⁸ , T. R. Geballe¹⁹ , Aarynn Carter⁴ , Katelyn Allers²⁰ , James Mang¹ , Dániel Apai^{2,10} , Mary Anne Limbach²¹ , and Mikayla J. Wilson⁴

¹ University of Texas at Austin, Department of Astronomy, 2515 Speedway C1400, Austin, TX 78712, USA; mrowland@utexas.edu

² Steward Observatory, University of Arizona, Tucson, AZ 85721, USA

³ Department of Astrophysics, American Museum of Natural History, New York, NY 10024, USA

⁴ Department of Astronomy and Astrophysics, University of California, Santa Cruz, Santa Cruz, CA 95064, USA

⁵ Ritter Astrophysical Research Center, Department of Physics and Astronomy, University of Toledo, 2801 West Bancroft Street, Toledo, OH 43606, USA

⁶ School of Earth Space Exploration, Arizona State University, Tempe, AZ 85287, USA

⁷ NASA Goddard Space Flight Center, Greenbelt, MD 20771, USA

⁸ School of Physics, Trinity College Dublin, The University of Dublin, Dublin 2, Ireland

⁹ Department of Physics, Graduate Center, City University of New York, 365 5th Avenue, New York, NY 10016, USA

¹⁰ Lunar and Planetary Laboratory, University of Arizona, Tucson, AZ, USA

¹¹ Centre for Astrophysics Research, Department of Physics, Astronomy and Mathematics, University of Hertfordshire, Hatfield AL10 9AB, UK

¹² SETI Institute, Mountain View, CA, USA

¹³ Space Science and Astrobiology Division, NASA Ames Research Center, Moffett Field, CA 94035, USA

¹⁴ Bay Area Environmental Research Institute, Moffett Field, CA 94035, USA

¹⁵ Eureka Scientific, Inc., Oakland, CA 94602, USA

¹⁶ Dordt University, Sioux Center, IA 51250, USA

¹⁷ Space Science Institute, Boulder, CO 80301, USA

¹⁸ United States Naval Observatory Flagstaff Station, Flagstaff, AZ, USA

¹⁹ Gemini Observatory/NSF's NOIRLab, Hilo, HI 96720, USA

²⁰ Bucknell University, Lewisburg, PA 17837, USA

²¹ Department of Astronomy, University of Michigan, Ann Arbor, MI 48109, USA

Received 2024 August 26; revised 2024 November 20; accepted 2024 November 25; published 2024 December 18

Abstract

The coldest Y spectral type brown dwarfs are similar in mass and temperature to cool and warm (~200–400 K) giant exoplanets. We can therefore use their atmospheres as proxies for planetary atmospheres, testing our understanding of physics and chemistry for these complex, cool worlds. At these cold temperatures, their atmospheres are cold enough for water clouds to form, and chemical timescales increase, increasing the likelihood of disequilibrium chemistry compared to warmer classes of planets. JWST observations are revolutionizing the characterization of these worlds with high signal-to-noise, moderate-resolution near- and mid-infrared spectra. The spectra have been used to measure the abundances of prominent species, like water, methane, and ammonia; species that trace chemical reactions, like carbon monoxide; and even isotopologues of carbon monoxide and ammonia. Here, we present atmospheric retrieval results using both published fixed-slit (Guaranteed Time Observation program 1230) and new averaged time series observations (GO program 2327) of the coldest known Y dwarf, WISE 0855–0714 (using NIRSpec G395M spectra), which has an effective temperature of ~264 K. We present a detection of deuterium in an atmosphere outside of the solar system via a relative measurement of deuterated methane (CH₃D) and standard methane. From this, we infer the D/H ratio of a substellar object outside the solar system for the first time. We also present a well-constrained part-per-billion abundance of phosphine (PH₃). We discuss our interpretation of these results and the implications for brown dwarf and giant exoplanet formation and evolution.

Unified Astronomy Thesaurus concepts: [Planetary atmospheres \(1244\)](#); [Brown dwarfs \(185\)](#); [Y dwarfs \(1827\)](#); [Exoplanet atmospheres \(487\)](#); [Exoplanet atmospheric composition \(2021\)](#)

1. Introduction

Brown dwarfs are the lowest-mass product of the stellar initial mass function and typically form like stars via gravitational collapse within molecular clouds (K. L. Luhman et al. 2007;

²² 51 Pegasi b Fellow.

Original content from this work may be used under the terms of the [Creative Commons Attribution 4.0 licence](#). Any further distribution of this work must maintain attribution to the author(s) and the title of the work, journal citation and DOI.

M. R. Bate 2019). This formation mechanism can produce objects with a large range of masses, from hydrogen-burning stars with masses $>70 M_{\text{Jup}}$, to deuterium-burning objects with masses between ~ 12 and $70 M_{\text{Jup}}$, to objects with masses $<12 M_{\text{Jup}}$ that do not undergo any type of fusion (C. V. Morley et al. 2024). Objects with masses $>\sim 12 M_{\text{Jup}}$ achieve deuterium fusion in their cores for at least part of their history. In brown dwarfs, deuterium fusion ceases due to either failure to maintain dense and hot enough cores to sustain fusion or exhaustion of the deuterium fuel (D. S. Spiegel et al. 2011; C. V. Morley et al. 2024). These deuterium- and hydrogen-burning limits are metallicity-dependent

and decrease with increasing metallicity (C. V. Morley et al. 2024). In any case, after fusion stops, these objects progress through spectral types L, T, and finally Y as they cool (J. D. Kirkpatrick 2005; M. C. Cushing et al. 2011). Because brown dwarfs must have cooled to their current temperatures within a Hubble time, thermo-evolutionary models such as those of D. Saumon & M. S. Marley (2008) and M. W. Phillips et al. (2020) suggest that the coldest of the Y dwarfs must be objects with masses $<12 M_{\text{Jup}}$ that never underwent deuterium fusion.

Observations of deuterium have a long history of informing planet formation, migration, and evolution theories within the solar system starting with the detection and abundance measurement of deuterated methane (CH_3D) in Jupiter (R. Beer et al. 1972; R. Beer & F. W. Taylor 1973). Deuterium has the potential to be a mass indicator for larger objects. Nevertheless, there have been no detections of deuterium in any extrasolar atmosphere to date (C. V. Morley et al. 2019). Other isotopes, like those of carbon, oxygen, and nitrogen, have been detected in atmospheres of exoplanets and brown dwarfs by several ground- and space-based moderate- to high-resolution near-infrared spectrographs (M. R. Line et al. 2021; Y. Zhang et al. 2021a, 2021b; D. Barrado et al. 2023; L. Finnerty et al. 2023, 2024; S. Gandhi et al. 2023; D. González Picos et al. 2024; C. E. Hood et al. 2024; B. W. P. Lew et al. 2024; P. C. B. Smith et al. 2024; J. W. Xuan et al. 2024a, 2024b). P. Mollière & I. A. G. Snellen (2019) have proposed that these isotopes can be used as an additional tracer of planet formation for objects in disks; however, more work connecting these isotopic species to disk theory needs to be done to determine how these species can trace an object’s formation mechanism, formation location, and migration (E. A. Bergin et al. 2024).

1.1. Deuterium as a Mass Indicator

Brown dwarfs are fully convective below their radiative-convective atmospheres (A. Burrows et al. 1997; G. Chabrier & I. Baraffe 2000). The presence of deuterated species in the atmosphere means the object did not fuse all of its deuterium, so its presence can be used as a mass indicator. Evolutionary models by D. S. Spiegel et al. (2011) and C. V. Morley et al. (2024) show that the deuterium-burning limit varies with metallicity, helium abundance, and cloud properties, and that objects greater than $\sim 12 M_{\text{Jup}}$ will fuse a fraction ($>50\%$) of their deuterium and objects greater than $20 M_{\text{Jup}}$ will fuse all of their deuterium within the first 100 Myr. The presence of deuterium in the atmospheres of all but the youngest objects would indicate that those objects’ masses are below the deuterium-burning limit.

1.2. Deuterium in the Solar System

The ratio of deuterium to hydrogen (D/H) can trace volatile transport within a system in addition to subsequent atmospheric evolution through atmospheric escape. The D/H ratio among comets is enhanced by an order of magnitude over D/H values in the interstellar medium (ISM) due to the preferred form of water ice being deuterated water (HDO) rather than H_2O at temperatures below 50 K (L. I. Cleves et al. 2014). This enhancement at cold temperatures would also affect the icy mantles of pebbles in the early outer solar system. The D/H ratio of the Earth is similar to that of comets, and S. Ida et al. (2019) showed that Earth’s deuterium enhancement could be explained under the pebble accretion theory if some of the

pebbles were transported to the inner solar system before the formation of Jupiter opened a gap in the disk and halted pebble migration. E. D. Young et al. (2023) showed that some of the Earth’s water and a fraction of the Earth’s HDO could also be formed via room-temperature reactions between FeO in an early magma ocean and a primordial hydrogen-dominated atmosphere. This would suggest that Earth’s deuterium abundance is due to multiple processes and only partially attributable to the transport of volatiles within a system.

The D/H ratios in the Martian and Venutian atmospheres are enhanced by several orders of magnitude over the Earth’s value because of the preferential depreciation of lighter hydrogen atoms over heavier deuterium atoms in atmospheric loss processes (M. J. Drake 2005). The D/H ratio of the ice giants is also enhanced because they accreted deuterium-enriched ices during formation, and large fractions of their envelopes are comprised of these ices (H. Feuchtgruber et al. 2013). While the gas giants Saturn and Jupiter also accreted these ices, their envelopes are dominated by helium and molecular hydrogen, so no enrichment is detected above the protosolar ratio ($1-2 \times 10^{-5}$; E. Lellouch et al. 2001).

1.3. Phosphine in Substellar Objects

Phosphine (PH_3) is the observed reservoir of phosphorous in gas giant planets in the solar system and is the expected reservoir of phosphorous in giant extrasolar atmospheres colder than ~ 1000 K (S. T. Ridgway et al. 1976; H. P. Larson et al. 1977, 1980). PH_3 has a significant absorption feature at $\sim 4.2 \mu\text{m}$ but has been difficult to detect at expected quantities in all cold atmospheres outside of the solar system (C. Visscher et al. 2006; C. V. Morley et al. 2018; S. A. Beiler et al. 2024b; J. K. Faherty et al. 2024; C. E. Hood et al. 2024; H. Kothari et al. 2024). Vertical mixing in cold atmospheres is expected to bring PH_3 from the warm interior into the photosphere. This effect has been seen on Jupiter ($T_{\text{eff}} = 125$ K), which has a PH_3 abundance of 1–2 ppm ($10^{-5.7}$ – 10^{-6} ; L. N. Fletcher et al. 2009). However, outside of a tentative detection from A. J. Burgasser et al. (2024), PH_3 has remained elusive in moderate- and high-resolution spectra of T dwarfs and low-resolution spectra of Y dwarfs down to $T_{\text{eff}} = 264$ K. In particular, vertical mixing rates inferred from measured CO abundances imply that large amounts of PH_3 should be detected in cold atmospheres (B. E. Miles et al. 2020). However, C. V. Morley et al. (2018) placed an upper limit of $<10^{-6.30}$ on the PH_3 abundance in the coldest brown dwarf, which is orders of magnitude less than the expected value.

1.4. WISE J085510.83–071442.5

WISE J085510.83–071442.5 (hereafter WISE 0855) is the coldest known brown dwarf, with $T_{\text{eff}} = 264$ K and an estimated mass of $3 M_{\text{Jup}} < M < 10 M_{\text{Jup}}$ (K. L. Luhman 2014; T. L. Esplin et al. 2016; S. K. Leggett et al. 2017, 2021; K. L. Luhman et al. 2024). It is the fourth-closest stellar or brown dwarf system to the Sun with a distance of just 2.28 pc (J. D. Kirkpatrick et al. 2021). Its Earth-like temperature and inferred planetary mass have made it a useful analog of temperate gas giant planets that are lacking in the solar system, since due to their lower masses, Jupiter and Saturn have both cooled to <150 K. A. J. Skemer et al. (2016) suggested that deuterium could be detected in the form of CH_3D , and C. V. Morley et al. (2019) calculated that a 10σ detection of CH_3D is possible with less than 2.5 hr of observations by the

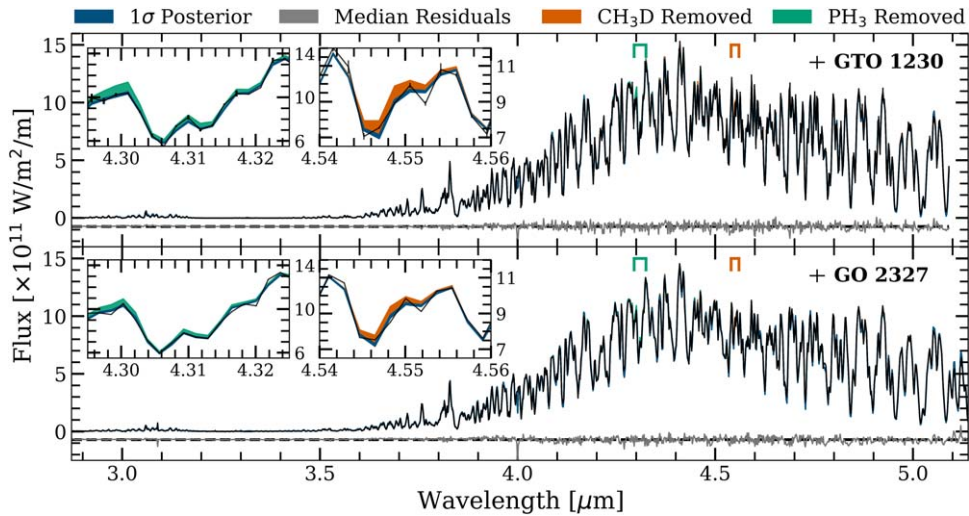


Figure 1. The JWST/NIRSpec G395M spectrum with error bars of WISE 0855 for GTO program 1230 (PI: Alves de Oliveira; top) and GO program 2327 (PI: Skemer; bottom); the 1σ retrieved spectrum and the residuals from the median retrieved spectrum are shown in black, blue, and gray. The differences between the best-fit spectrum and the best-fit spectrum with PH_3 or CH_3D opacity removed are plotted in shaded green and orange, respectively. The regions where each opacity has the largest effect on the spectrum ($\approx 10\%$) are highlighted in subpanels, showing that both PH_3 or CH_3D are detected in both data sets. The GTO data set has a mean S/N of 107, and the GO data set has a mean S/N of 759.

James Webb Space Telescope’s (JWST) moderate-resolution ($R \sim 2700$) G395H mode.

Here we present detections of CH_3D and PH_3 in WISE 0855 using two independent JWST NIRSpec/G395M ($R \sim 1000$) observations. These are the first simultaneous detection of deuterium and the first abundance measurement of PH_3 in an extrasolar atmosphere. We quantify the effective mixing timescale for PH_3 and calculate the D/H ratio for WISE 0855.

2. Methods

2.1. Observations and Data Reduction

Two independent WISE 0855 data sets reduced by different teams were used for the retrieval analysis. The first data set was taken as part of JWST Guaranteed Time Observation (GTO) program 1230 (PI: Alves de Oliveira) and published by K. L. Luhman et al. (2024). The details of that program and the reduction are provided in K. L. Luhman et al. (2024). Program 1230 observed WISE 0855 in the fixed-slit mode of JWST/NIRSpec with the G395M/F290LP grating/filter setting and a three-point dither pattern. The total exposure time was 15,200 s. The second data set is from General Observer (GO) program 2327 (PI: Skemer; Co-PIs: Morley and Miles). Program 2327 used the Bright Object Time Series mode of JWST/NIRSpec with the G395M/F290LP grating/filter combination and no dithering over 11 hr. We discuss the data reduction of program 2327 and differences with program 1230 in this section.

The weighted average spectrum covers 2.87–5.10 μm at a resolution of ~ 1000 . The observations started on 2023 December 2 at 01:03:18.92 UTC and ended on 2023 December 2 at 12:09:33.18 UTC. The 11 hr total exposure time was composed of 44 15 minute integrations. The observations were reduced using version 1.14.0 of the standard JWST pipeline (H. Bushouse et al. 2024) with CRDS version “11.17.20” and CRDS context “jwst_1215.pmap.” Stage 1 was run with the default parameters to correct detector-level artifacts and convert raw detector images into slope images. Stage 2 of the pipeline corrects residual detector artifacts at the integration level and converts slope images into flux-calibrated two-

dimensional spectral images. All default stage 2 steps are run with one additional step. The `nsclean` step was turned on to remove correlated read noise. The two-dimensional individual spectral images are then used for spectral extraction.

The 44 spectral images were split into six separate segment files. The first five segments each hold eight spectral images, and the last segment has four spectral images. The average two-dimensional spectral image is calculated for each segment and used to estimate the shape of the spectral trace. At every column (y-dimension), a one-dimensional Gaussian is fit to subpixel precision to estimate the center (in the x-dimension) of the trace. The x- and y-values are used to fit a second-order Chebyshev series to the spectral trace.²³ We defined an 8 pixel wide extraction aperture centered at the best fit at each column. The excess background at each column is estimated by taking a median of the 3 pixels outside of the extraction aperture from both sides. The median excess background is then subtracted off from the extracted spectrum.

Each spectral image has an associated error image and wavelength map. The same extraction radius is used to estimate the error using the standard error propagation and wavelength solution of each pixel. After all 44 spectra were extracted, they were visually compared to mask hot pixels and other outliers. The weighted average and propagated errors of all the masked spectra were calculated to produce a high signal-to-noise ratio (S/N) spectrum of WISE 0855 for retrieval analysis, shown in Figure 1.²⁴

Understanding the differences between the spectra presented in K. L. Luhman et al. (2024) and this work is challenging due to WISE 0855’s inherent variability and the ~ 9 month time difference between observations. Finding the differences between the pipeline used for the K. L. Luhman et al. (2024) spectrum and the standard JWST pipeline would be ideally addressed with nonvariable, standard sources but is beyond the scope of this work. For the purposes of the retrieval analysis, the reductions from K. L. Luhman et al. (2024) and this work

²³ Example: <https://github.com/exonik/JWebbinar2023-TSO/blob/main/Part2-Spec2.ipynb>.

²⁴ The JWST data used in this analysis can be found in MAST: 10.17909/rjtp-zn54.

are treated as two different epochs. Additional discussion of the reductions is included in Appendix A.

2.2. Retrieval

We performed a suite of retrievals on the spectra using the GPU-enabled CHIMERA retrieval framework (M. R. Line et al. 2015). All models used the radiative transfer code described in C. E. Hood et al. (2023), which adapted the GPU-enabled radiative transfer from J. A. Zalesky et al. (2022) to solve the two-stream multiple scattering problem using the methods from O. B. Toon et al. (1989). We utilized the Anaconda Numba `guvectorize` framework on NVIDIA A100 GPUs. The GPU memory (40 GB) limited the number of simultaneous CPU threads to four. Like the previously mentioned studies, parameter estimation was conducted using the `emcee` package (D. Foreman-Mackey et al. 2013). All retrievals used a minimum of eight walkers per parameter, were run to 60,000 iterations, and took approximately 40 hr. Initial `emcee` walker positions in parameter space were constructed using a Gaussian ball centered on by-eye fits informed by Sonora Elf Owl models (S. Mukherjee et al. 2024).

We modified the free temperature–pressure profile described in M. R. Line et al. (2015) to directly retrieve the temperature at 18 points equally spaced in \log_{10} pressure between -4.3 and 2.5 to ensure the capture of any potential temperature inversion above 1 mbar, as seen in J. K. Faherty et al. (2024).

We included the following gas opacities: H_2O (O. L. Polyansky et al. 2018), CH_4 (R. J. Hargreaves et al. 2020), CH_3D (R. J. Hargreaves et al. 2020), ^{12}CO (L. S. Rothman et al. 2010; G. Li et al. 2015), ^{13}CO (L. S. Rothman et al. 2010; G. Li et al. 2015), CO_2 (X. Huang et al. 2014), NH_3 (S. N. Yurchenko et al. 2011), H_2S (J. Tennyson & S. N. Yurchenko 2012; A. A. Azzam et al. 2015), and PH_3 (J. Tennyson & S. N. Yurchenko 2012; C. Sousa-Silva et al. 2015) as well as $\text{H}_2\text{--H}_2$ and $\text{H}_2\text{--He}$ collision-induced opacities. We did not include HDO because its expected opacity is several orders of magnitude below the dominant opacity sources at all observed wavelengths. We assume uniform-with-altitude mixing ratios. We include nongray H_2O clouds using the EDDYSED model with a lognormal particle size distribution and three retrieved values (cloud base pressure, sedimentation efficiency f_{sed} , and cloud volume mixing ratio, VMR; A. S. Ackerman & M. S. Marley 2001). Additional retrievals with a nonuniform-with-altitude mixing ratio for H_2O were performed using the method described in M. J. Rowland et al. (2023). CH_3D cross sections were scaled to terrestrial abundances (6.227×10^{-4} or 1:1606 relative to CH_4). We retrieve the log of the CH_3D abundance relative to the terrestrial $\text{CH}_3\text{D}/\text{CH}_4$ ratio.

Models were run at a variable resolution ranging from $R \sim 18,000$ at shorter wavelengths to $R \sim 35,000$ at longer wavelengths to ensure a constant 25 model points per instrumental resolution across the entire wavelength range ($2.9\text{--}5.55 \mu\text{m}$). Model spectra were rotationally broadened according to a $v \sin i$ parameter, Doppler-shifted according to a radial velocity parameter, convolved to the instrumental resolution of G395M (~ 2.2 pixels per resolution element), and binned.

Additional retrievals with different chemistry profile, temperature profile, cloud, and rotational broadening treatments were performed. All parameters and their prior ranges are provided in Table 1, and a list of all retrievals performed is provided in Table 2. Some parameters (e.g., surface gravity, radius, and abundance profiles) were retrieved directly, while

other bulk properties, like the $P(T)$ profile, effective temperature, metallicity, and C/O, were derived based on retrieved parameters. These derivations are described below.

To calculate the effective temperature, we equate Boltzmann’s law to the bolometric flux between 0.77 and $30 \mu\text{m}$, similar to the method used in M. R. Line et al. (2017).

Metallicity is computed as

$$[\text{M}/\text{H}] = \log_{10} \left(\frac{(\text{M}/\text{H})_{\text{retrieved}}}{(\text{M}/\text{H})_{\text{solar}}} \right), \quad (1)$$

where the retrieved metallicity is taken to be the summation of the elemental species included in the retrieval model. The C/O ratio is computed as

$$\frac{\text{C}}{\text{O}} = \frac{\sum \text{C}}{\sum \text{O}} \approx \frac{\text{CH}_4 + \text{CH}_3\text{D} + ^{12}\text{CO} + ^{13}\text{CO} + \text{CO}_2}{1.22 \times (\text{H}_2\text{O} + ^{12}\text{CO} + ^{13}\text{CO} + 2\text{CO}_2)}. \quad (2)$$

E. Calamari et al. (2024) found a median atmospheric oxygen sink of 17.8% $^{+1.7\%}_{-2.3\%}$ for brown dwarfs in the solar neighborhood due to oxygen sequestration into silicate clouds deep below the photosphere. This corresponds to an oxygen correction of $1.22^{+0.02}_{-0.04}$, as shown in Equation (2). This correction does not account for any oxygen that may be sequestered in water clouds.

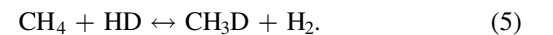
CH_3D was retrieved as the \log_{10} ratio of $\text{CH}_3\text{D}/\text{CH}_4$ relative to the terrestrial ratio (1:1606), with a broad prior of -3 to 3 (corresponding to a CH_3D abundance of 1/1000 to $1000 \times$ terrestrial). To calculate the abundance of CH_3D , we used the following equation:

$$f_{\text{CH}_3\text{D}} = f_{\text{CH}_4} \times C_E \times f_{\text{CH}_3\text{D}/\text{CH}_4}, \quad (3)$$

where $f_{\text{CH}_3\text{D}}$ is the VMR of CH_3D , f_{CH_4} is the VMR of CH_4 , C_E is 6.227×10^{-4} (the $\text{CH}_3\text{D}/\text{CH}_4$ of Earth), and $f_{\text{CH}_3\text{D}/\text{CH}_4}$ is the unlogged retrieved ratio. The D/H ratio as measured in CH_3D is computed as

$$(\text{D}/\text{H})_{\text{CH}_4} = \frac{\sum \text{D}}{\sum \text{H}} \approx \frac{\text{CH}_3\text{D}}{4\text{CH}_4 + 3\text{CH}_3\text{D}}. \quad (4)$$

The D/H ratio of H_2 in the envelope, $(\text{D}/\text{H})_{\text{H}_2}$, is taken to be the bulk D/H ratio of the object. This assumption is valid if the components were well mixed at least once in the object’s history, as would be the case if WISE 0855 is a low-mass product of the initial mass function. However, the D/H ratio is not inferred from a HD/ H_2 measurement but by the $\text{CH}_3\text{D}/\text{CH}_4$ measurement, $(\text{D}/\text{H})_{\text{CH}_4}$. The chemical reaction that produces CH_3D in an atmosphere is



The fractionation factor that describes the ratio of $(\text{D}/\text{H})_{\text{CH}_4}$ to $(\text{D}/\text{H})_{\text{H}_2}$ is described in C. Lecluse et al. (1996). It decreases with increasing CH_3D quench temperature until reaching a value of 1.0 at quench temperatures >1200 K. Jupiter has a CH_3D quench temperature of 790 K and a measured fractionation factor of 1.25, with lower quench temperatures and higher fractionation factors for the colder planets (B. Fegley & R. G. Prinn 1988; C. Lecluse et al. 1996). We do not have a robust constraint on the CH_3D quench temperature in WISE 0855, so we estimate a fractionation factor between 1.0 and 1.1 based on extrapolations from the solar system fractionation factors.

The inclusion of each trace gas species adds one parameter to the model. To assess whether the additional parameter is warranted (i.e., improves the model fit to the data), we computed the Bayesian information criterion (BIC) for each

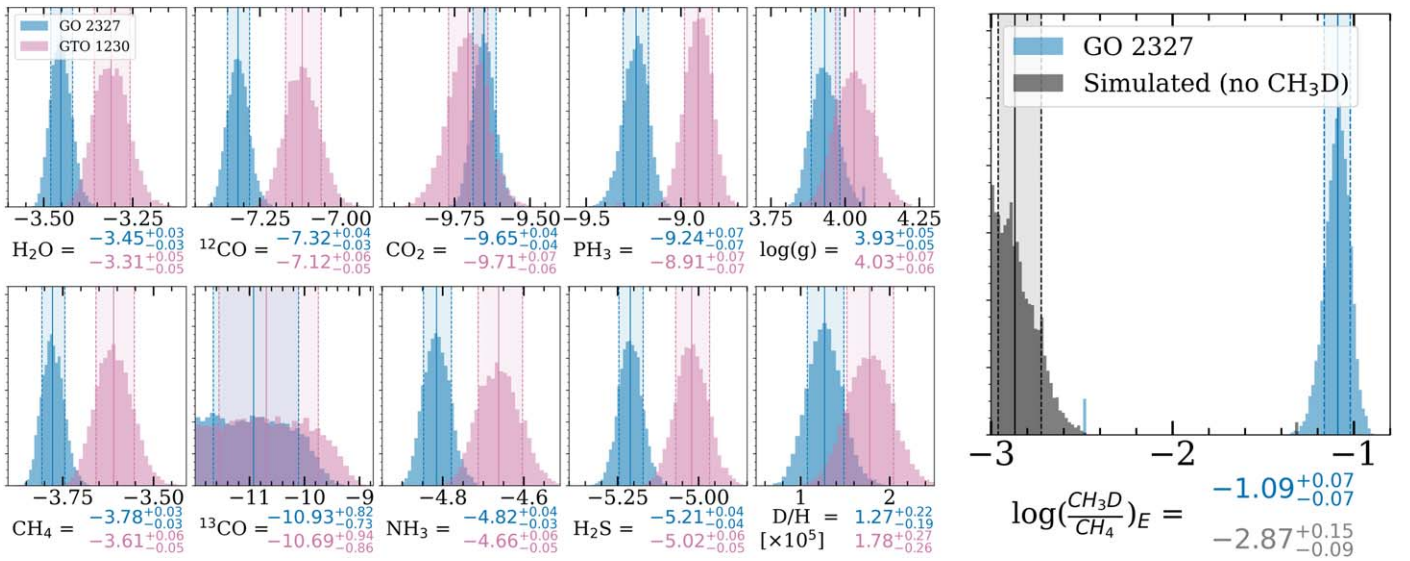


Figure 2. Left panel: the retrieved posteriors for the gas-phase abundances and $\log(g)$ for the GTO spectrum (pink) and GO spectrum (blue). All gases are constrained with the exception of ¹³CO. Right panel: the retrieved $\log(\frac{\text{CH}_3\text{D}}{\text{CH}_4})_E$ posterior from the GO spectrum (blue) and a simulated spectrum based on the best-fit model with CH₃D opacity set to 0. The bounded constraint from the actual data and the upper limit from the synthetic data indicate that CH₃D information exists in NIRSPEC/G395M data.

retrieval. The BIC was computed as

$$\text{BIC} = -2\ln(L) + \ln(N)K, \quad (6)$$

where $\ln(L)$ is the log likelihood of the best-fit model, N is the number of data points, and K is the number of parameters. The model with the lower BIC indicates the better model. We select between two models using the following intervals used in R. E. Kass & A. E. Raftery (1995) with evidence against the higher BIC as $0 < \Delta\text{BIC} < 2$: no preference worth mentioning; $2 < \Delta\text{BIC} < 6$: positive; $6 < \Delta\text{BIC} < 10$: strong; and $10 < \Delta\text{BIC}$: very strong.

3. Results

Spectra retrieved for both the GTO program 1230 (PI: Alves de Oliveira, hereafter ‘‘GTO data’’) data set published by K. L. Luhman et al. (2024) and the averaged time series observations from GO program 2327 (PI: Skemer, hereafter ‘‘GO data’’) are presented in Figure 1.

Retrieved gas abundances and $\log(g)$ are shown in Figure 2, and the derived parameters and the $P(T)$ profiles are shown in Figure 3. While the retrieved $P(T)$ profiles differ from the self-consistent Elf Owl model, they generally agree with each other and the self-consistent model in the photosphere. Both retrievals show these deviations despite a smoothing hyperparameter that may be due to inhomogeneities like patchy cloud cover or other three-dimensional effects.

We calculated the bolometric luminosity (L_{bol}) using the PRISM spectrum published in K. L. Luhman et al. (2024) and the method described in S. A. Beiler et al. (2024a) and determine a $\log L/L_{\odot} = -7.297 \pm 0.042$, which agrees with the $\log L/L_{\odot} = -7.305 \pm 0.020$ calculated in K. L. Luhman et al. (2024). We calculated a $T_{\text{eff}} = 264 \pm 8$ K using an assumed age of 1–10 Gyr to estimate the radius from evolutionary models (M. S. Marley et al. 2021), which is slightly colder than the $T_{\text{eff}} = 285$ K determined by model fitting in K. L. Luhman et al. (2024).

In the GO data set (GTO data set) we retrieve subsolar metallicity $[\text{M}/\text{H}] = -0.33 \pm 0.03$ (-0.18 ± 0.05), a C/O ratio

of 0.39 ± 0.01 (0.41 ± 0.01) compared to a solar C/O of 0.48, and $\log(g) = 3.93 \pm 0.05$ (4.03 ± 0.07). We find that the G395M spectra do not have sufficient resolution to constrain $v \sin i$. We derive a slightly higher $T_{\text{eff}} = 293_{-3}^{+5}$ K (286_{-3}^{+4}) compared to the T_{eff} expected from $L_{\text{bol}} = 264 \pm 8$. We derive a mass of $2.48_{-0.22}^{+0.27} M_{\text{Jup}}$ ($2.17_{-0.27}^{+0.31} M_{\text{Jup}}$). Both the high T_{eff} and low mass are driven by the low retrieved $R = 0.85_{-0.01}^{+0.02} R_{\text{Jup}}$ (0.70 ± 0.02), a common problem with brown dwarf retrievals (J. A. Zalesky et al. 2019; E. C. Gonzales et al. 2020; D. Kitzmann et al. 2020; B. Burningham et al. 2021). K. L. Luhman et al. (2024) estimated a radius of $0.9 R_{\text{Jup}}$, and evolutionary models predict a radius between 0.97 and $1.1 R_{\text{Jup}}$ (M. S. Marley et al. 2021). Assuming $R = 1.0 R_{\text{Jup}}$, we recalculate a mass of $3.44 M_{\text{Jup}}$ ($4.33 M_{\text{Jup}}$) based on the retrieved scale factor and $\log(g)$.

While many of the bulk properties retrieved in each data set qualitatively agree, we note that some parameters, like some gas abundances and the radius, disagree by more than 1σ . We note that abundance ratios tend to be more robust than individual abundances, with our retrieved C/O and CH₃D/CH₄ ratios agreeing within 1σ . The difference in radius may be due to differences in the data reduction pipelines used for each data set. WISE 0855 is a variable object, and observations were taken 9 months apart. If this variability is driven by clouds, clouds may impact the gas-phase abundances of prominent opacity sources like H₂O. Finally, the GTO observations spanned 1 hr, and the GO observations spanned 11 hr and covered all or most of a rotation period. If spatial or temporal inhomogeneities exist, they may have impacted each data set differently. The impact of these factors on retrieved posteriors will be explored in a future work.

3.1. CH₃D Detection

Using the high-S/N time series observations, we retrieve a $\log_{10} \text{CH}_3\text{D}/\text{CH}_4$ of $-1.09_{-0.07}^{+0.06}$ relative to terrestrial ratios, which corresponds to a $(\text{D}/\text{H})_{\text{CH}_4}$ of $1.27_{-0.19}^{+0.22} \times 10^{-5}$ and a bulk D/H ratio of $1.15_{-0.17}^{+0.34} \times 10^{-5}$, assuming a fractionation factor between 1.0 and 1.1. Using the GTO observations, we retrieve a slightly larger $(\text{D}/\text{H})_{\text{CH}_4}$ of $1.78_{-0.26}^{+0.27} \times 10^{-5}$ and a

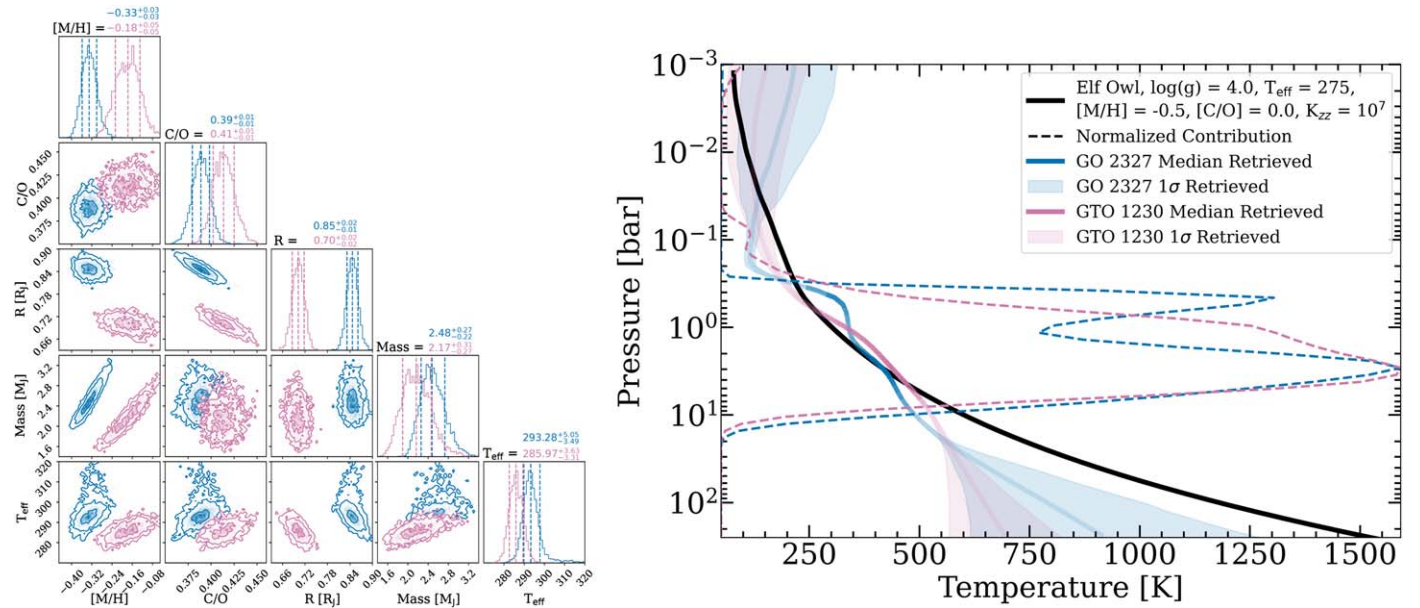


Figure 3. The corner plot of derived parameters and the $P(T)$ profile of the fiducial retrieval on the GTO spectrum (pink) and the time-averaged GO spectrum (blue). The dashed lines in the $P(T)$ plot show the normalized flux-averaged contribution for each layer in the atmosphere, and the opaqueness of the $P(T)$ profile corresponds to this value, with a minimum of 20% for visibility.

bulk D/H of $1.62^{+0.43}_{-0.24} \times 10^{-5}$. These values agree within 1σ of the GTO results and are roughly consistent with a protosolar ratio of $1\text{--}2 \times 10^{-5}$. These retrieved values are robust to all model parameterizations tested and are listed in Appendix B. The retrieved D/H values were invariant to walkers initialized with Gaussian balls centered on a terrestrial abundance (a high $\text{CH}_3\text{D}/\text{CH}_4$ abundance) and $1/1000$ th of a terrestrial abundance (a very low $\text{CH}_3\text{D}/\text{CH}_4$ abundance). The retrieved D/H value did not change within the 1σ errors for retrievals with H_2O Mie scattering clouds or no clouds, with uniform-with-pressure chemistry abundance profiles for all gases (including H_2O), with a nonuniform profile for H_2O , with a smoothed or unsmoothed $P(T)$ profile, or with the FastRotBroad and the Rot Broad Int rotational broadening functions.

We performed retrievals without CH_3D to test the strength of our detection. The models with CH_3D opacity were strongly preferred, with a ΔBIC value of -44.9 in the GO data set and a ΔBIC value of -55.4 in the GTO data set.

To bolster confidence in the CH_3D detection, we performed an injection and retrieval test similar to the method in M. R. Line et al. (2021). We created a synthetic data set using our best-fit model from the GO data set retrieval but with CH_3D opacity removed. We added synthetic noise by sampling each data point from a normal distribution characterized by the error bar at each wavelength. We then performed a retrieval including CH_3D as a parameter and only retrieved an upper limit. The results are shown in Figure 2. The bounded constraint from the actual data and the upper limit from the synthetic data indicate that CH_3D information exists in NIRSpec/G395M data and is sufficient to constrain the CH_3D abundance.

3.2. PH_3 Detection

We also detect PH_3 in both data sets. In the GO data set, we detect a $\log_{10}(\text{VMR})$ abundance of -9.24 ± 0.07 , and in the GTO data set, we detect a $\log_{10}(\text{VMR})$ abundance of -8.91 ± 0.07 . Similarly to the CH_3D tests described in the previous section, we performed retrievals with and without PH_3 . The models with PH_3 were strongly preferred over those

without with a ΔBIC value of -27.9 in the GO data set and a ΔBIC value of -61.9 in the GTO data set. We performed a cross-correlation analysis following the methods of Y. Zhang et al. (2021b), in which the residuals of the best-fit model with PH_3 opacity removed and a PH_3 model are cross-correlated. This resulted in a cross-correlation function (CCF) S/N of 8.5. The results of this analysis are included in Appendix B.

4. Discussion

The detection of deuterium in WISE 0855 and the inference of a mass below $12 M_{\text{Jup}}$ agree with theoretical cooling models from D. Saumon & M. S. Marley (2008) and M. W. Phillips et al. (2020) that predict a mass between 3 and $10 M_{\text{Jup}}$ for ages between 1 and 10 Gyr.

4.1. Prospect for CH_3D Detection in Exoplanets and Brown Dwarfs

C. V. Morley et al. (2019) predicted that an $R \sim 2700$ spectrum with $\text{S/N} > 40$ would be sufficient to detect CH_3D in a $T_{\text{eff}} = 300$ K atmosphere. Here we have shown that CH_3D is detectable in $R \sim 1000$ spectra with $\text{S/N} > 100$. CH_3D should be detectable in cold, isolated Y dwarfs in this mass range with moderate-resolution spectra from JWST at the above S/N.

We removed all CH_3D opacity from the best-fit model to the GO data set to determine its impact on the G395M spectra and the spectral S/N needed to detect CH_3D . The removal of CH_3D affected the flux most strongly between 4.31 and $4.67 \mu\text{m}$. Its removal caused a flux difference $>0.5\%$ (corresponding to an $\text{S/N} = 200$) in 58 pixels, $>1\%$ ($\text{S/N} = 100$) in 20 pixels, and $>1.5\%$ ($\text{S/N} = 67$) in 10 pixels. Other molecular opacity sources in the 4.31 to $4.67 \mu\text{m}$ range include CO_2 at the bluer wavelengths and CO at the redder wavelengths. As CO becomes the dominant carbon reservoir (through a hotter effective temperature or more vigorous vertical mixing), CH_3D features become less observable.

The detection of deuterium in an atmosphere outside of the solar system with JWST opens several intriguing possibilities for planet

characterization and our understanding of planetary formation. The absorption strengths of both CH_3D and HDO increase relative to those of their nondeuterated counterparts at colder temperatures, and their detection becomes more difficult as the temperature of the planet increases. Cold, faint exoplanets are difficult to observe, but P. Mollière & I. A. G. Snellen (2019) have shown that CH_3D is detectable in exoplanets with the Extremely Large Telescope (ELT) and that HDO is potentially detectable in exoplanets with JWST if strong vertical mixing removes most of the CH_4 from the photosphere. Additionally, C. V. Morley et al. (2019) found that CH_3D is detectable for any cold (≈ 320 K), young (< 20 Myr) Neptunes discovered with JWST. Since deuterium is easier to detect in higher-metallicity atmospheres, a S/N ratio of 5 would be sufficient to detect a protosolar abundance of deuterium in a young Neptune twin ($[M/H] = 2.0$). The D/H ratios as a function of object mass for objects in the solar system, low-mass brown dwarf models, and this work are shown in Figure 4.

Additionally, a higher D/H ratio, and thus a higher $\text{CH}_3\text{D}/\text{CH}_4$ or $\text{HDO}/\text{H}_2\text{O}$ ratio, makes deuterium easier to detect. These ratios would be inflated in an atmosphere that has undergone significant atmospheric mass loss that preferentially loses the lighter hydrogen over the heavier deuterium. P. Mollière & I. A. G. Snellen (2019) predict that HDO in a nontransiting GJ 1214 b twin at half the distance to Earth and a D/H ratio of 3×10^{-4} is observable with the ELT. P.-G. Gu & H. Chen (2023) and C. Cherubim et al. (2024) have predicted that HDO may be observable for several irradiated, deuterium-enriched sub-Neptunes.

Unfortunately, a large portion of the most detectable HDO band ($3.6 \mu\text{m} < \lambda < 4.0 \mu\text{m}$) as described in P. Mollière & I. A. G. Snellen (2019), C. V. Morley et al. (2019), and G. Chabrier et al. (2000) is in the G395H/S200A1 detector gap ($3.69 \mu\text{m} < \lambda < 3.79 \mu\text{m}$) or the G395H/S200A2 detector gap ($3.81 \mu\text{m} < \lambda < 3.92 \mu\text{m}$). However, P. Mollière & I. A. G. Snellen (2019) determined that HDO is still detectable with only $3.60\text{--}3.80 \mu\text{m}$ spectra, so G395H/S200A2 may be preferred if using the highest-resolution mode of JWST. G395M, the lower-resolution mode of JWST/NIRSpec, does not have this gap and may be more useful in capturing the entire HDO band.

4.2. Isotopologues and Their Potential for Tracing Planet Formation

Beginning with the detections of ^{13}CO in the directly imaged, widely separated substellar object TYC 8998 b by Y. Zhang et al. (2021a) and in the isolated brown dwarf 2MASS J03552337+1133437 by Y. Zhang et al. (2021b), isotopologue detections in brown dwarf and exoplanet atmospheres have become possible due to new ground- and space-based moderate- and high-resolution infrared spectrographs. Subsequent $^{12}\text{CO}/^{13}\text{CO}$ has been determined (or had an upper limit determined) for several brown dwarfs (C. E. Hood et al. 2024; B. W. P. Lew et al. 2024; J. W. Xuan et al. 2024a) and exoplanets (M. R. Line et al. 2021; L. Finnerty et al. 2023, 2024; S. Gandhi et al. 2023; D. González Picos et al. 2024; P. C. B. Smith et al. 2024; J. W. Xuan et al. 2024b), with ratios appearing lower for objects that formed in disks compared to those that did not. JWST has enabled detections of other isotopologues such as $^{15}\text{NH}_3$ in D. Barrado et al. (2023) and C^{17}O and/or C^{18}O in S. Gandhi et al. (2023) and D. González Picos et al. (2024). This work is the first to detect the isotope deuterium in an extrasolar atmosphere.

Isotopologues, particularly those involving ^{13}C and deuterium, have been detected in disks for decades (A. Dutrey et al. 1994;

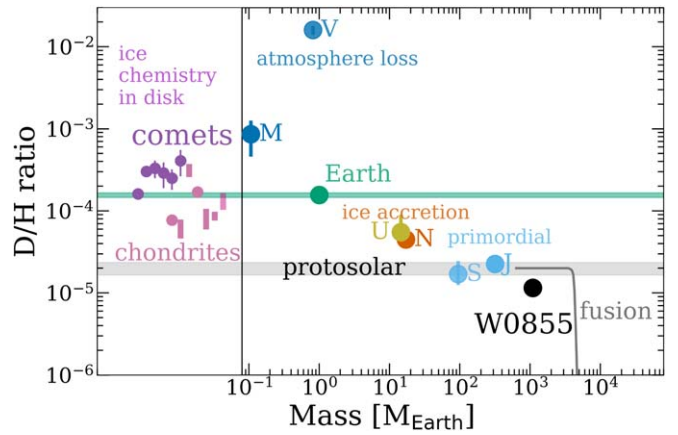


Figure 4. D/H ratio as a function of object mass as measured in the ISM (gray), terrestrial planets, ice giants, gas giants (M. J. Drake 2005; P. Hartogh et al. 2011; L. I. Cleeves et al. 2014), and brown dwarfs as predicted from D. S. Spiegel et al. (2011; dark gray line), with the retrieved D/H measurement of WISE 0855 in black. The mass estimate is derived from the retrieved $\log(g)$ with a radius of $1.0 R_{\text{Jup}}$.

E. A. Bergin et al. 2013; S. Guilloteau et al. 2013; J. Huang et al. 2017; J. J. Tobin et al. 2023; L. Podio et al. 2024). The differing optical depths of ^{13}CO and ^{12}CO allow them to be used to probe different parts of the disk. If future disk observations and modeling can determine isotopologue ratios as a function of separation, they can act as a planet formation and migration tracer alongside traditional tracers like carbon and oxygen.

4.3. PH_3 and Chemical Disequilibrium

We detect approximately 1 ppb of PH_3 in the atmosphere of WISE 0855. At the cold temperature of this Y dwarf, we expect the presence of disequilibrium gas species with abundances quenched at higher values found deeper in the atmosphere. While the rest of the gas abundances are consistent with rapid vertical mixing of $\log(K_{zz}) > 7 \text{ cm}^2 \text{ s}^{-1}$, the low abundance of PH_3 appears consistent with chemical equilibrium or very slow mixing ($\log(K_{zz}) < 2$). The abundance of PH_3 reported here, the previously reported nondetections of PH_3 , and the predicted abundances from S. Mukherjee et al. (2022) as a function of T_{eff} and $\log(K_{zz})$ are shown in Figure 5.

Our measured PH_3 abundance of $10^{-8.91}$ in the previously published K. L. Luhman et al. (2024) data set and $10^{-9.24}$ in the GO data set are consistent with the modeling in K. L. Luhman et al. (2024), which found that a PH_3 abundance of 10^{-8} produced too strong an absorption feature to fit their data. Based on *L*-band ($3.4\text{--}4.14 \mu\text{m}$) and *M*-band ($4.5\text{--}5.1 \mu\text{m}$) spectra from A. J. Skemer et al. (2016), C. V. Morley et al. (2018) placed an upper limit on PH_3 of $10^{-6.30}$ for this object. B. E. Miles et al. (2020) found an underabundance of PH_3 in WISE 0855 compared to the amount predicted by the vertical mixing timescale inferred from CO abundances ($\log(K_{zz}) = 8.5$).

Our $\log(K_{zz})$ values inferred from our retrieved CO abundance (> 7) and PH_3 abundance (< 2) are discrepant. Our inference of slow vertical mixing depends on the accuracy of the phosphorus thermochemical timescales of L. V. Gurvich et al. (1989). The number of nondetections shown in Figure 5 and the large number of nondetections in hotter T dwarfs not shown indicate that our knowledge of phosphorous chemistry is incomplete. The low but constrained abundance in WISE 0855 adds information that will hopefully aid in the identification of problematic elements in the phosphorous chemical reaction timescale network.

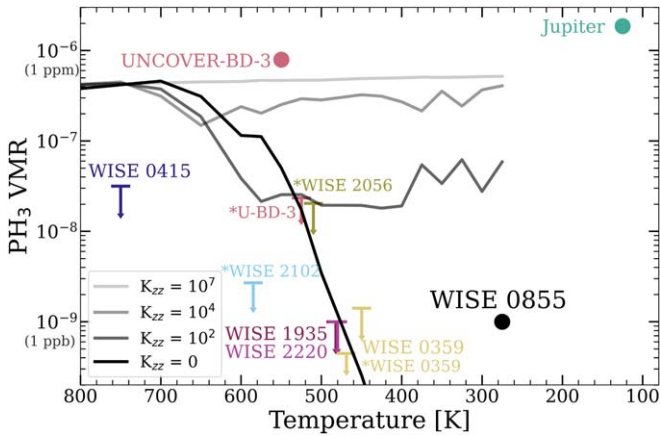


Figure 5. The PH_3 abundance as a function of T_{eff} for Y dwarfs with detections or upper limits from S. A. Beiler et al. (2024a), A. J. Burgasser et al. (2024), J. K. Faherty et al. (2024), C. E. Hood et al. (2024), H. Kothari et al. (2024), and this work, along with the global PH_3 abundance of Jupiter from L. N. Fletcher et al. (2009). The * indicates recalculated upper limits from S. A. Beiler et al. (2024a). The gray and black lines show the Elf Owl PH_3 abundance at 3 bars for various mixing strengths and effective temperatures. All models assume $\log(g) = 4$, cloud-free, solar metallicity, and solar C/O atmospheres. Models extend down to 275 K. WISE 0855 is consistent with very slow ($\log(K_{zz}) < 2 \text{ cm}^2 \text{ s}^{-1}$) mixing.

A. J. Burgasser et al. (2024) made the first claim of PH_3 in an extrasolar atmosphere based on $4.2 \mu\text{m}$ absorption in the NIRSpec/PRISM spectra of UNCOVER-BD-3, a cold ($T_{\text{eff}} = 550 \text{ K}$), low-metallicity ($[M/H] = -1.0$) Y dwarf with potential halo membership. Recent work by S. A. Beiler et al. (2024b) highlighted the difficulty in disentangling PH_3 absorption from CO_2 with forward model fitting due to the overabundance of PH_3 and underabundance of CO_2 in current models. They were not able to rule out PH_3 in UNCOVER-BD-3 but found that the $4.2 \mu\text{m}$ feature could be explained by excess CO_2 compared to model predictions.

5. Conclusions

Here we report a detection of a deuterated gas species, CH_3D , and a part-per-billion level abundance of PH_3 in the atmosphere of the coldest brown dwarf, WISE 0855. These detections highlight the extreme sensitivity of JWST. Our CH_3D and PH_3 abundances were retrieved in two independent data sets reduced by different groups and were robust to a variety of model assumptions. Models with CH_3D and PH_3 opacities were strongly preferred over models without them. An injection and retrieval test indicates that the CH_3D information present in NIRSpec/G395M spectra is sufficient to constrain the CH_3D abundance. A cross-correlation analysis of the residuals detected PH_3 at a CCF S/N of 8.5. Differences in the posteriors of other parameters may be driven by single-epoch versus averaged time series observations and will be explored in a future work.

We derive a protosolar D/H ratio from an abundance of CH_3D retrieved in JWST NIRSpec/G395M spectra. The presence of deuterium in the atmosphere of a free-floating object indicates that WISE 0855 has a mass less than the deuterium-burning limit of $\sim 12 M_{\text{Jup}}$, in agreement with evolutionary models. It also underscores the opportunity JWST presents to find this powerful formation tracer in exoplanet atmospheres, as predicted by P. Mollière & I. A. G. Snellen (2019) and C. V. Morley et al. (2019).

Acknowledgments

We would like to acknowledge Elena Manjavacas for her expertise and advice on the ESA and STSci pipelines. We would like to acknowledge Stephan Birkmann for advice on the ESA pipeline and providing intermediate data products. We would like to acknowledge the JWST Helpdesk Team and Lonestar6 at the Texas Advanced Computing Center (TACC) at the University of Texas at Austin. Support for programs JWST-AR-01977.004 and JWST-GO-02124.009-A were provided by NASA through a grant from the Space Telescope Science Institute, which is operated by the Association of Universities for Research in Astronomy, Incorporated, under NASA contract NAS5-26555. This material is based on work supported by the National Aeronautics and Space Administration under grant No. 80NSSC21K0650 for the NNN20ZDA001N-ADAP:D.2 program. M.J.R. acknowledges funding from NASA FINESST grant No. 80NSSC20K1550. C. V.M. acknowledges support from the Alfred P. Sloan Foundation under grant number FG-2021-16592. C.V.M. acknowledges the National Science Foundation, which supported the work presented here under grant No. 1910969. B.E.M. was supported by the Heising-Simons Foundation 51 Pegasi b Postdoctoral Fellowship. J.F. acknowledges funding from the Heising-Simons Foundation as well as NSF award #2238468 and #1909776 and NASA award #80NSSC22K0142 J.M.V. acknowledges support from a Royal Society—Science Foundation Ireland University Research Fellowship (URF\R1\221932). B.B. acknowledges support from the UK Research and Innovation Science and Technology Facilities Council [ST/X001091/1]. R.L. acknowledges support from STSci grant No. JWST-GO-02327. E.G.N. & N. B. acknowledge support from the NASA XRP funding NNN21ZDA001N-XRP.

Software: CHIMERA (M. R. Line et al. 2013), emcee (D. Foreman-Mackey et al. 2013), corner.py (D. Foreman-Mackey 2016).

Appendix A Data Set Comparison

The K. L. Luhman et al. (2024) spectrum was reduced using a custom pipeline developed by the European Space Agency NIRSpec science operations team, which adopts the same algorithms included in the standard JWST pipeline, except for a correction for “snowballs” and a correction for residual correlated noise²⁵ (C. Alves de Oliveira et al. 2018; P. Ferruit et al. 2022; T. Böker et al. 2023). The median percent difference of the K. L. Luhman et al. (2024) spectrum from our spectrum between 4.00 and $5.09 \mu\text{m}$ is on average 4%, with a standard deviation of 13%. We show the differences between both reductions over the region where CH_3D is detected in Figure 6. Most of the differences seen between the two reductions can be explained by the inherent variability in the GO data. We believe the outliers to be a result of different data reduction pipelines, which is beyond the scope of this Letter. The data from the GTO program were also rereduced using the standard JWST pipeline through stages 1–3 with the same CRDS version and context as the time series data. When using the same raw detector files, the median ratio between the spectrum produced by the NIRSpec science operations team pipeline and the standard JWST pipeline is 11% with a standard deviation of 14%.

²⁵ <https://www.cosmos.esa.int/web/jwst-nirspec/technical-notes>

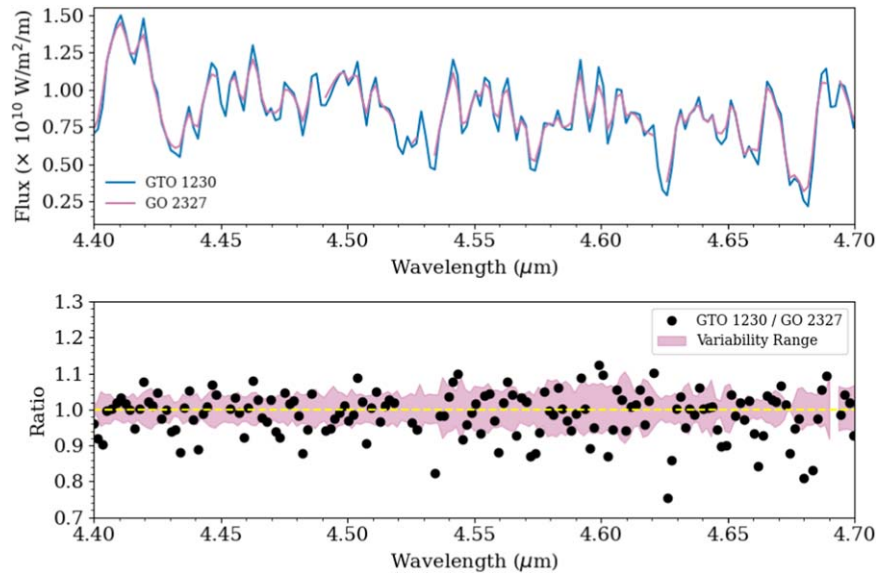


Figure 6. Comparison of reduced spectra within the region most impacted by CH_3D absorption. Top panel: the GTO spectrum (blue) plotted with the GO spectrum (pink). The GO spectrum is interpolated onto the same wavelength grid as the GTO spectrum. Bottom panel: the ratio of the GTO spectrum divided by the GO spectrum (black dots). The yellow dashed line is a reference for no difference. The top of the pink area is the ratio of the brightest spectrum divided by the dimmest spectrum in the time series. The bottom of the pink area is the dimmest spectrum divided by the brightest spectrum.

Appendix B

List of Retrievals and Retrieved Parameters

In most retrievals, model spectra were rotationally broadened using the `fastRotBroad` function from `PyAstronomy` as in C. E. Hood et al. (2023, 2024) (S. Czesla et al. 2019). `fastRotBroad` was found by J. W. Xuan et al. (2024b) to be invalid over a large wavelength range, so additional retrievals were performed using `RotBroadInt` from A. Carvalho & C. M. Johns-Krull (2023). Retrievals performed with `RotBroadInt` took an average of 69.5 hr compared to 34.5 hr for retrievals with `fastRotBroad`. The G395M spectra were insufficient to accurately constrain $v \sin i$ values, and the use of the `RotBroadInt` function did not change other retrieved values. All parameters and their prior ranges are provided in Table 1, and a list of all retrievals performed is provided in Table 2. We attribute the discrepancy in the retrieved radial velocities between the two data sets to different wavelength calibrations between the two pipelines.

A subset of retrieved posteriors is provided in Figure 7. Retrieved $\log_{10}(\frac{\text{CH}_3\text{D}}{\text{CH}_4})_E$ values remained consistent across all retrievals performed on the same data set. The retrieved error bar inflation parameter was also consistent for all retrievals performed on the same data set. Other bulk properties remained consistent across retrievals, with the exception of the nonuniform H_2O retrieval, which retrieved $\log_{10}(\text{H}_2\text{O})$ abundances of -3.12 ± 0.07 in the deep atmosphere and -3.40 ± 0.05 in the upper atmosphere. We used the deep atmosphere abundance to calculate $[\text{M}/\text{H}] = -0.06 \pm 0.07$ and $\text{C}/\text{O} = 0.24 \pm 0.02$. The two additional parameters needed for the nonuniform H_2O profile did not appreciably improve the fit, and the model was not preferred. All cloud models assumed H_2O Mie scattering clouds. We retrieved an upper limit for the cloud VMR (see Figure 7), and the other cloud parameters were unconstrained across the performed retrievals. We do not draw conclusions about the presence or absence of water clouds, but these results indicate that clouds modeled with Mie scattering and lognormal particle size distributions may not be sufficient to fit the spectra of cold objects.

Table 1
Retrieved Parameters

Parameter	Description	Prior
$\log_{10}(g)$	\log_{10} of surface gravity (cm s^{-2})	$M < 100 M_{\text{Jup}}$
$(R/D)^2$	radius-to-distance scale factor ($R_{\text{Jup}} \text{ pc}^{-1}$)	$0 < (R/D)^2 < 1$
10^b	Error bar inflation	$0.01 \times (\sigma_{\text{min}}^2)$, $100 \times (\sigma_{\text{min}}^2)$
T_i	Temperature (K) at a given pressure level	$< 4000 \text{ K}$
γ	$P(T)$ profile smoothing hyperparameter	$0 - \infty$
$\log_{10}(f_i)$	\log_{10} of the VMR of a uniform gas	$> -12, \sum F_i < 1$
$\log_{10}(\frac{\text{CH}_3\text{D}}{\text{CH}_4})_E$	\log_{10} ratio relative to terrestrial (1/1606)	-3 to 3
$\log_{10}(C)$	\log_{10} of the cloud VMR	-15 to 0
$\log_{10}(P_c)$	\log_{10} of the cloud base pressure	-15 to 0
f_{sed}	Sedimentation efficiency	$0 - 10$
RV	Radial velocity (km s^{-1})	-50 to 50
$v \sin i$	Rotational velocity (km s^{-1})	$0 - 140$

We followed the method described in Y. Zhang et al. (2021b) to perform a cross-correlation analysis to test the detection of CH_3D and PH_3 . Our CCF used the residuals (the observed spectrum minus the best-fit model with CH_3D or PH_3 opacity removed) and the CH_3D or PH_3 model spectrum. This model spectrum was created by subtracting the best-fit spectrum from the same model but with the targeted opacity set to 0. The CCF was then normalized by its standard deviation outside of the peak within the velocity of $[-10,000, -800]$ and $[800, 10,000]$. This CCF is shown in Figure 7 and results in a CCF S/N of 3.8 for CH_3D and a CCF S/N of 8.5 for PH_3 . We note the prominent troughs and inconclusive result of the CH_3D CCF. We attribute this to the narrow wavelength range of the most prominent CH_3D feature and the relatively low ($R \sim 1000$) resolution of NIRSpc/G395M.

Table 2
List of Retrievals

Data	Clouds	$P(T)$	H ₂ O	Broadening	CH ₃ D	PH ₃	Parameters	$\log_{10}(\frac{\text{CH}_3\text{D}}{\text{CH}_4})_E$	ΔBIC
GO	Yes	Smoothed	Uniform	FastRotBroad	Yes	Yes	36	$-1.09^{+0.06}_{-0.07}$	N/A
GO	Yes	Smoothed	Uniform	FastRotBroad	No	Yes	35	N/A	-44.9
GO	Yes	Smoothed	Uniform	FastRotBroad	Yes	No	35	$-1.10^{+0.09}_{-0.10}$	-27.9
GO	None	Smoothed	Uniform	FastRotBroad	Yes	Yes	33	$-1.10^{+0.06}_{-0.07}$	N/A
GO	None	Smoothed	Uniform	FastRotBroad	No	Yes	32	N/A	-44.1
GO	Yes	Unsmoothed	Uniform	FastRotBroad	Yes	Yes	35	$-1.02^{+0.06}_{-0.06}$	N/A
GO	Yes	Unsmoothed	Uniform	FastRotBroad	No	Yes	34	N/A	-55.7
GO	Yes	Smoothed	Uniform	RotBroadInt	Yes	Yes	36	$-1.09^{+0.06}_{-0.07}$	N/A
GO	Yes	Smoothed	Uniform	RotBroadInt	No	Yes	35	N/A	-42.8
GO	Yes	Smoothed	Nonuniform	RotBroadInt	Yes	Yes	38	$-1.14^{+0.10}_{-0.07}$	N/A
GO	Yes	Smoothed	Nonuniform	RotBroadInt	No	Yes	37	N/A	-18.3
GTO	Yes	Smoothed	Uniform	FastRotBroad	Yes	Yes	36	$-0.94^{+0.06}_{-0.07}$	N/A
GTO	Yes	Smoothed	Uniform	FastRotBroad	No	Yes	35	N/A	-55.4
GTO	Yes	Smoothed	Uniform	FastRotBroad	Yes	No	35	$-0.92^{+0.06}_{-0.07}$	-61.9

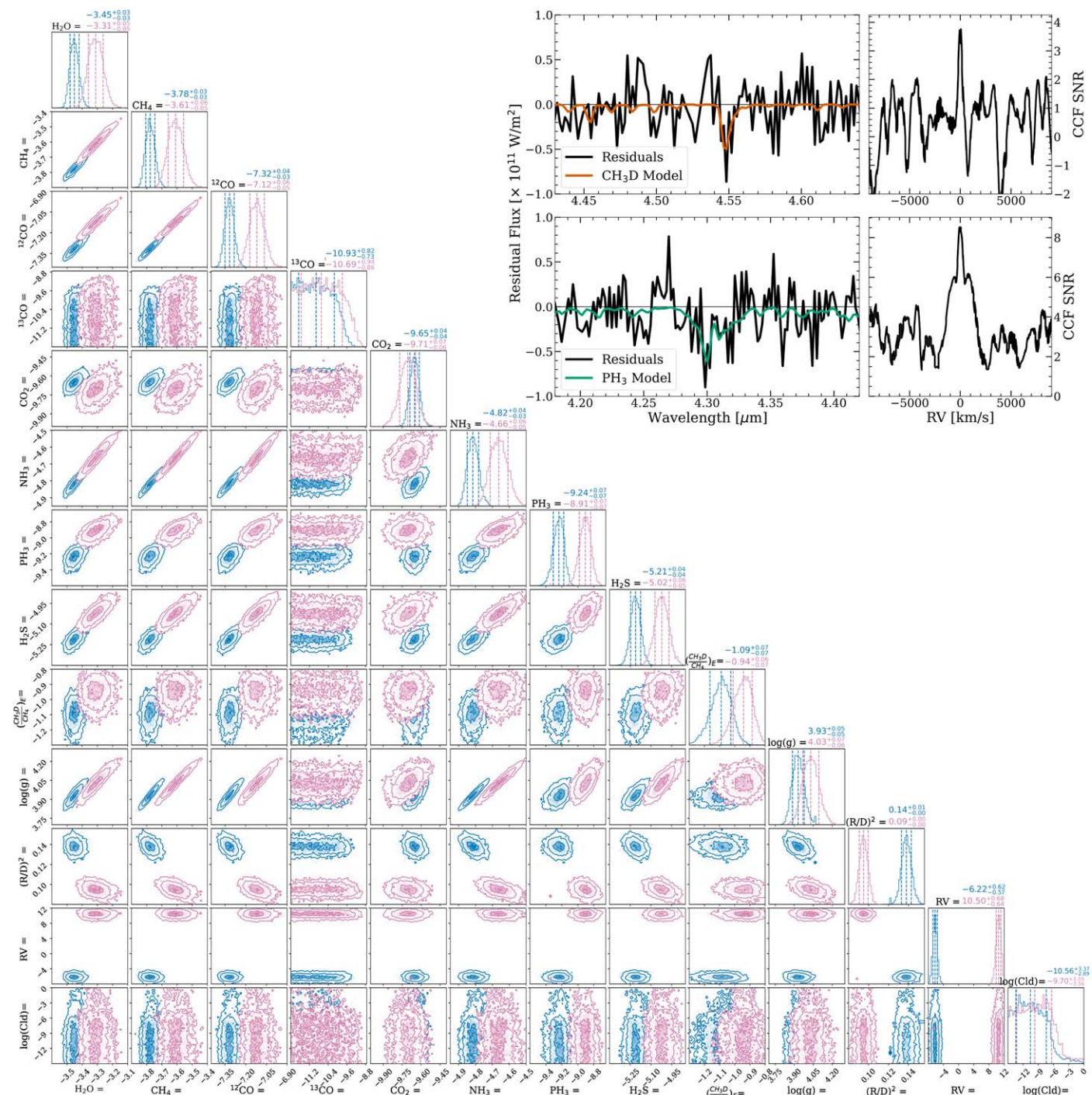










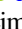




Figure 7. The corner plot of a subset of retrieved parameters from the GTO spectrum (pink) and the time-averaged GO spectrum (blue). The discrepancy between the retrieved radial velocities is believed to be due to differences in wavelength calibration in the two pipelines. An upper limit for the cloud VMR is shown, and other cloud parameters were unconstrained. Top panel: the CCF computed for the GO data set with the CH₃D model (top) or PH₃ model (bottom) and residuals (observed spectrum minus the best-fit model with the relevant opacity removed). The CCF is normalized by the standard deviation outside of the CCF peak so that the y-axes of the right-hand panels represent the S/N of the CCF peak.

ORCID iDs

Melanie J. Rowland <https://orcid.org/0000-0003-4225-6314>
 Caroline V. Morley <https://orcid.org/0000-0002-4404-0456>
 Brittany E. Miles <https://orcid.org/0000-0002-5500-4602>
 Genaro Suarez <https://orcid.org/0000-0002-2011-4924>
 Jacqueline K. Faherty <https://orcid.org/0000-0001-6251-0573>
 Andrew J. Skemer <https://orcid.org/0000-0001-6098-3924>
 Samuel A. Beiler <https://orcid.org/0000-0002-6721-1844>

Michael R. Line <https://orcid.org/0000-0002-2338-476X>
 Gordon L. Bjoraker <https://orcid.org/0000-0002-9679-4153>
 Jonathan J. Fortney <https://orcid.org/0000-0002-9843-4354>
 Johanna M. Vos <https://orcid.org/0000-0003-0489-1528>
 Sherelyn Alejandro Merchan <https://orcid.org/0000-0003-0548-0093>
 Mark Marley <https://orcid.org/0000-0002-5251-2943>
 Ben Burningham <https://orcid.org/0000-0003-4600-5627>

Richard Freedman  <https://orcid.org/0000-0001-9333-4306>
 Ehsan Gharib-Nezhad  <https://orcid.org/0000-0002-4088-7262>
 Natasha Batalha  <https://orcid.org/0000-0003-1240-6844>
 Roxana Lupu  <https://orcid.org/0000-0003-3444-5908>
 Channon Visscher  <https://orcid.org/0000-0001-6627-6067>
 Adam C. Schneider  <https://orcid.org/0000-0002-6294-5937>
 T. R. Geballe  <https://orcid.org/0000-0003-2824-3875>
 Aarynn Carter  <https://orcid.org/0000-0001-5365-4815>
 Katelyn Allers  <https://orcid.org/0000-0003-0580-7244>
 James Mang  <https://orcid.org/0000-0001-5864-9599>
 Dániel Apai  <https://orcid.org/0000-0003-3714-5855>
 Mary Anne Limbach  <https://orcid.org/0000-0002-9521-9798>
 Mikayla J. Wilson  <https://orcid.org/0000-0003-3008-1975>

References

- Ackerman, A. S., & Marley, M. S. 2001, *ApJ*, 556, 872
 Alves de Oliveira, C., Birkmann, S. M., Böker, T., et al. 2018, *Proc. SPIE*, 10704, 107040Q
 Azzam, A. A. A., Lodi, L., Yurchenko, S. N., & Tennyson, J. 2015, *JQSRT*, 161, 41
 Barrado, D., Mollière, P., Patapis, P., et al. 2023, *Natur*, 624, 263
 Bate, M. R. 2019, *MNRAS*, 484, 2341
 Beer, R., Farmer, C. B., Norton, R. H., Martonchik, J. V., & Barnes, T. G. 1972, *Sci*, 175, 1360
 Beer, R., & Taylor, F. W. 1973, *ApJ*, 179, 309
 Beiler, S. A., Cushing, M. C., Kirkpatrick, J. D., et al. 2024a, *ApJ*, 973, 107
 Beiler, S. A., Mukherjee, S., Cushing, M. C., et al. 2024b, *ApJ*, 973, 60
 Bergin, E. A., Bosman, A., Teague, R., et al. 2024, *ApJ*, 965, 147
 Bergin, E. A., Cleeves, L. I., Gorti, U., et al. 2013, *Natur*, 493, 644
 Böker, T., Beck, T. L., Birkmann, S. M., et al. 2023, *PASP*, 135, 038001
 Burgasser, A. J., Bezanson, R., Labbe, I., et al. 2024, *ApJ*, 962, 177
 Burningham, B., Faherty, J. K., Gonzales, E. C., et al. 2021, *MNRAS*, 506, 1944
 Burrows, A., Marley, M., Hubbard, W. B., et al. 1997, *ApJ*, 491, 856
 Bushouse, H., Eisenhamer, J., Dencheva, N., et al. 2024, JWST Calibration Pipeline, v1.15.1, Zenodo, doi:10.5281/zenodo.12692459
 Calamari, E., Faherty, J. K., Visscher, C., et al. 2024, *ApJ*, 963, 67
 Carvalho, A., & Johns-Krull, C. M. 2023, *RNAAS*, 7, 91
 Chabrier, G., & Baraffe, I. 2000, *ARA&A*, 38, 337
 Chabrier, G., Baraffe, I., Allard, F., & Hauschildt, P. 2000, *ApJL*, 542, L119
 Cherubim, C., Wordsworth, R., Hu, R., & Shkolnik, E. 2024, *ApJ*, 967, 139
 Cleeves, L. I., Bergin, E. A., Alexander, C. M. O., et al. 2014, *Sci*, 345, 1590
 Cushing, M. C., Kirkpatrick, J. D., Gelino, C. R., et al. 2011, *ApJ*, 743, 50
 Czesla, S., Schröter, S., Schneider, C. P., et al. 2019, PyA: Python Astronomy-related Packages, Astrophysics Source Code Library, ascl:1906.010
 Drake, M. J. 2005, *M&PS*, 40, 519
 Dutrey, A., Guilloteau, S., & Simon, M. 1994, *A&A*, 286, 149
 Esplin, T. L., Luhman, K. L., Cushing, M. C., et al. 2016, *ApJ*, 832, 58
 Faherty, J. K., Burningham, B., Gagné, J., et al. 2024, *Natur*, 628, 511
 Fegley, B., & Prinn, R. G. 1988, *ApJ*, 326, 490
 Ferruit, P., Jakobsen, P., Giardino, G., et al. 2022, *A&A*, 661, A81
 Feuchtgruber, H., Lellouch, E., Orton, G., et al. 2013, *A&A*, 551, A126
 Finnerty, L., Schofield, T., Sappéy, B., et al. 2023, *AJ*, 166, 31
 Finnerty, L., Xuan, J. W., Xin, Y., et al. 2024, *AJ*, 167, 43
 Fletcher, L. N., Orton, G. S., Teanby, N. A., & Irwin, P. G. J. 2009, *Icar*, 202, 543
 Foreman-Mackey, D. 2016, *JOSS*, 1, 24
 Foreman-Mackey, D., Hogg, D. W., Lang, D., & Goodman, J. 2013, *PASP*, 125, 306
 Gandhi, S., de Regt, S., Snellen, I., et al. 2023, *ApJL*, 957, L36
 Gonzales, E. C., Burningham, B., Faherty, J. K., et al. 2020, *ApJ*, 905, 46
 González Picos, D., Snellen, I. A. G., de Regt, S., et al. 2024, *A&A*, 689, A212
 Gu, P.-G., & Chen, H. 2023, *ApJL*, 953, L27
 Guilloteau, S., Di Folco, E., Dutrey, A., et al. 2013, *A&A*, 549, A92
 Gurvich, L. V., Veits, I. V., & Alcock, C. B. 1989, Thermodynamics Properties of Individual Substances. Volume 1—Elements O, H/D, T/, F, Cl, Br, I, He, Ne, Ar, Kr, Xe, Rn, S, N, P, and Their Compounds. Part 1—Methods and Computation. Part 2—Tables (4th ed.; New York: Hemisphere Publishing Corporation)
 Hargreaves, R. J., Gordon, I. E., Rey, M., et al. 2020, *ApJS*, 247, 55
 Hartogh, P., Lis, D. C., Bockelée-Morvan, D., et al. 2011, *Natur*, 478, 218
 Hood, C. E., Fortney, J. J., Line, M. R., & Faherty, J. K. 2023, *ApJ*, 953, 170
 Hood, C. E., Mukherjee, S., Fortney, J. J., et al. 2024, arXiv:2402.05345
 Huang, J., Öberg, K. I., Qi, C., et al. 2017, *ApJ*, 835, 231
 Huang, X., Gamache, R. R., Freedman, R. S., Schwenke, D. W., & Lee, T. J. 2014, *JQSRT*, 147, 134
 Ida, S., Yamamura, T., & Okuzumi, S. 2019, *A&A*, 624, A28
 Kass, R. E., & Raftery, A. E. 1995, *JASA*, 90, 773
 Kirkpatrick, J. D. 2005, *ARA&A*, 43, 195
 Kirkpatrick, J. D., Gelino, C. R., Faherty, J. K., et al. 2021, *ApJS*, 253, 7
 Kitzmann, D., Heng, K., Oreshenko, M., et al. 2020, *ApJ*, 890, 174
 Kothari, H., Cushing, M. C., Burningham, B., et al. 2024, *ApJ*, 971, 121
 Larson, H. P., Fink, U., Smith, H. A., & Davis, D. S. 1980, *ApJ*, 240, 327
 Larson, H. P., Treffers, R. R., & Fink, U. 1977, *ApJ*, 211, 972
 Lecluse, C., Robert, F., Gautier, D., & Guiraud, M. 1996, *P&SS*, 44, 1579
 Leggett, S. K., Tremblin, P., Esplin, T. L., Luhman, K. L., & Morley, C. V. 2017, *ApJ*, 842, 118
 Leggett, S. K., Tremblin, P., Phillips, M. W., et al. 2021, *ApJ*, 918, 11
 Lellouch, E., Bézard, B., Fouchet, T., et al. 2001, *A&A*, 370, 610
 Lew, B. W. P., Roellig, T., Batalha, N. E., et al. 2024, *AJ*, 167, 237
 Li, G., Gordon, I. E., Rothman, L. S., et al. 2015, *ApJS*, 216, 15
 Line, M. R., Brogi, M., Bean, J. L., et al. 2021, *Natur*, 598, 580
 Line, M. R., Marley, M. S., Liu, M. C., et al. 2017, *ApJ*, 848, 83
 Line, M. R., Teske, J., Burningham, B., Fortney, J. J., & Marley, M. S. 2015, *ApJ*, 807, 183
 Line, M. R., Wolf, A. S., Zhang, X., et al. 2013, *ApJ*, 775, 137
 Luhman, K. L. 2014, *ApJL*, 786, L18
 Luhman, K. L., Joergens, V., Lada, C., et al. 2007, in Protostars and Planets V, ed. B. Reipurth, D. Jewitt, & K. Keil (Tucson, AZ: Univ. of Arizona Press), 443
 Luhman, K. L., Tremblin, P., Alves de Oliveira, C., et al. 2024, *AJ*, 167, 5
 Marley, M. S., Saumon, D., Visscher, C., et al. 2021, *ApJ*, 920, 85
 Miles, B. E., Skemer, A. J. I., Morley, C. V., et al. 2020, *AJ*, 160, 63
 Mollière, P., & Snellen, I. A. G. 2019, *A&A*, 622, A139
 Morley, C. V., Skemer, A. J., Allers, K. N., et al. 2018, *ApJ*, 858, 97
 Morley, C. V., Skemer, A. J., Miles, B. E., et al. 2019, *ApJL*, 882, L29
 Morley, C. V., Mukherjee, S., Marley, M. S., et al. 2024, *ApJ*, 975, 59
 Mukherjee, S., Fortney, J. J., Batalha, N. E., et al. 2022, *ApJ*, 938, 107
 Mukherjee, S., Fortney, J. J., Morley, C. V., et al. 2024, *ApJ*, 963, 73
 Phillips, M. W., Tremblin, P., Baraffe, I., et al. 2020, *A&A*, 637, A38
 Podio, L., Ceccarelli, C., Codella, C., et al. 2024, *A&A*, 688, L22
 Polyansky, O. L., Kyuberis, A. A., Zobov, N. F., et al. 2018, *MNRAS*, 480, 2597
 Ridgway, S. T., Wallace, L., & Smith, G. R. 1976, *ApJ*, 207, 1002
 Rothman, L. S., Gordon, I. E., Barber, R. J., et al. 2010, *JQSRT*, 111, 2139
 Rowland, M. J., Morley, C. V., & Line, M. R. 2023, *ApJ*, 947, 6
 Saumon, D., & Marley, M. S. 2008, *ApJ*, 689, 1327
 Skemer, A. J., Morley, C. V., Allers, K. N., et al. 2016, *ApJL*, 826, L17
 Smith, P. C. B., Line, M. R., Bean, J. L., et al. 2024, *AJ*, 167, 110
 Sousa-Silva, C., Al-Refaie, A. F., Tennyson, J., & Yurchenko, S. N. 2015, *MNRAS*, 446, 2337
 Spiegel, D. S., Burrows, A., & Milsom, J. A. 2011, *ApJ*, 727, 57
 Tennyson, J., & Yurchenko, S. N. 2012, *MNRAS*, 425, 21
 Tobin, J. J., van't Hoff, M. L. R., Leemker, M., et al. 2023, *Natur*, 615, 227
 Toon, O. B., McKay, C. P., Ackerman, T. P., & Santhanam, K. 1989, *JGR*, 94, 16287
 Visscher, C., Lodders, K., & Fegley, B. J. 2006, *ApJ*, 648, 1181
 Xuan, J. W., Hsu, C.-C., Finnerty, L., et al. 2024a, *ApJ*, 970, 71
 Xuan, J. W., Wang, J., Finnerty, L., et al. 2024b, *ApJ*, 962, 10
 Young, E. D., Shahar, A., & Schlichting, H. E. 2023, *Natur*, 616, 306
 Yurchenko, S. N., Barber, R. J., & Tennyson, J. 2011, *MNRAS*, 413, 1828
 Zalesky, J. A., Line, M. R., Schneider, A. C., & Patience, J. 2019, *ApJ*, 877, 24
 Zalesky, J. A., Saboi, K., Line, M. R., et al. 2022, *ApJ*, 936, 44
 Zhang, Y., Snellen, I. A. G., Bohn, A. J., et al. 2021a, *Natur*, 595, 370
 Zhang, Y., Snellen, I. A. G., & Mollière, P. 2021b, *A&A*, 656, A76